Mechanistic grain growth model for fresh and irradiated UO$_2$ nuclear fuel

Michael R. Tonks [a],*, Pierre-Clément A. Simon [b], Jacob Hirschhorn [a]

[a] *Department of Material Science and Engineering, University of Florida, Gainesville, FL 32611, United States*
[b] *Ken and Mary Alice Lindquist Department of Nuclear Engineering, The Pennsylvania State University, University Park, PA 16802, United States*

ARTICLE INFO

ABSTRACT

The purpose of this work is to develop a mechanistic model of grain growth in UO$_2$ fuel during reactor operation. The model development builds on published experimental data on UO$_2$ grain growth, as well as atomistic and mesoscale simulation results. We begin by developing new fits with temperature T (in K) for the average grain boundary (GB) energy and mobility in UO$_2$ using literature data, where the GB energy $\bar{\gamma} = (1.56 - 5.87 \times 10^{-4}T) \pm 0.3$ J/m^2 and the GB mobility $\bar{M} = (2.14 \pm 0.15 \times 10^{-7}) \exp(-(290 \pm 22 \text{ kJ/mol})/RT)$ m^4/(Js). We then discuss the pinning of grain boundaries by porosity, including porosity left over after sintering and fission gas bubbles that form during operation. We present our mechanistic model and validate it using existing grain growth data. Finally, we implement the model in the BISON fuel performance code and quantify its impact for constant and transient power cases. Our model produces similar results to an empirical model for the constant power case, but it predicts more grain growth than the empirical model for the transient power case. We attribute this discrepancy to the new mechanistic model's ability to account for the impact of the temperature and power history.

© 2020 Elsevier B.V. All rights reserved.

1. Introduction

Grain growth plays a significant role in the life of light water reactor (LWR) uranium dioxide (UO$_2$) fuel pellets. During fuel pellet fabrication via sintering, the grain structure coarsens due to grain growth, resulting in an average grain size typically around ten microns. During reactor operation, significant grain growth occurs in the hotter portions of the fuel pellet, near its center, and the average grain size reaches several times its initial value. This change in grain size significantly impacts fuel performance, since the grain size affects various aspects of the overall behavior of the fuel, including fission gas release [1,2], fracture [3], and heat conduction [4].

The grain growth of UO$_2$ has been studied for many years, using both in- and out-of-pile experiments. The resultant data have significant scatter and have been analyzed in various ways [5,6]. The large scatter in the reported grain growth during thermal annealing of unirradiated UO$_2$ results from the sensitivity of grain growth to the stoichiometry, which is difficult to control, and to the porosity of the sintered samples. UO$_2$ grain growth becomes even more complicated during reactor operation. The stoichiometry changes, sintered porosity decreases, and solid fission products and fission gas bubbles form, all of which impact grain growth. Many semi-empirical models have been developed for grain growth in unirradiated UO$_2$ [5,6]. These depend on the initial grain size and the temperature but are independent of the porosity. Only a few semi-empirical models have been developed for in-reactor grain growth [5,7], and the oldest is still the most commonly used [5]. The predicted grain growth in this model is a function of initial grain size, temperature, and burnup.

Mechanistic models of grain growth explicitly describe the physical behaviors of grain boundary (GB) migration using parameters with real physical meaning, while semi-empirical models employ equations for which the form has some physical justification but includes parameters without physical meaning that are obtained by fitting to data. A major benefit of mechanistic models is that they can be applied to many materials, as long as the physical parameters are known. As far as the authors are aware, no mechanistic models have been developed to predict the change in the average grain size of UO$_2$ with time, though the semi-empirical model from Ainschough et al. [5] comes the closest. There have been a number of numerical simulation methods developed to model UO$_2$ grain growth at the mesoscale, in which the individual grains are resolved. Some have looked at pure curvature driven grain growth [8], while others have included additional driving forces [9] or pinning by porosity [10–13].

---

* Corresponding author.
E-mail address: michael.tonks@ufl.edu (M.R. Tonks).

In this work, we present a new, mechanistic model that predicts the increase in the average grain size for both unirradiated and irradiated UO_2. The average grain size is predicted as a function of the initial grain size, temperature, evolving sintered porosity, and fission gas bubble fractional coverage. The model parameters are the average GB energy and mobility in UO_2, as well as the pore mobility. In this paper, we begin by summarizing the relevant grain growth theory in Section 2. Then, in Section 3, we present new fits of data from the literature for the GB energy and mobility. We present our new mechanistic model in Section 4 and, in Section 5, validate it against experimental data. Finally, in Section 6, we implement the model in the BISON fuel performance code and quantify its impact on the predicted behavior for steady and transient power cases.

2. Grain growth theory

GBs migrate to reduce the overall free energy of the material. The velocity at a specific location on a GB v_g can be described as

$$v_g = M_g[F_g - P_g]^+, \tag{1}$$

where M_g is the GB mobility at the location, and F_g and P_g are the driving and resistive forces per unit area at the location, respectively. The $[x]^+$ operator is equal to x when $x > 0$ but is equal to zero when $x \leq 0$. Various driving forces for GB migration can occur, including GB energy, elastic energy, plastic energy, and temperature gradients. The GB energy driving force, often called the curvature driving force, is the most common, while the temperature gradient driving force has been found to be negligible for temperature gradients commonly experienced in both LWR and fast reactor oxide fuels [9]. The curvature driving force is defined as

$$F_g = \frac{\gamma_g}{R_g}, \tag{2}$$

where γ_g and R_g are the GB energy and radius of curvature at the GB location, respectively. The resistive force results from defects that impede GB migration, such as second phase particles or porosity. GB properties, such as the energy and mobility, are highly anisotropic, depending on the misorientation of grains on either side of the GB and on the inclination of the GB.

The migration of individual GBs causes some grains to shrink and disappear and others to grow. This results in an increase of the average grain size with time, commonly called grain growth. The GB anisotropy affects the motion of individual GBs and will impact which grains grow and shrink, but typically does not impact the average grain growth rate [14]. Therefore, when predicting the change in the average grain size, we can often neglect the anisotropy and focus on the average GB mobility and energy. If we consider a polycrystal in which the average grain size $\bar{D}$ and the average GB curvature $\bar{R}$ are related by a geometric constant α such that $\bar{D} = \alpha^{1/2}\bar{R}$, then the change in the average grain size with time is

$$\frac{\partial \bar{D}}{\partial t} = \alpha^{1/2}\frac{\partial \bar{R}}{\partial t} \approx \alpha \bar{M}\frac{\bar{\gamma}}{\bar{D}}, \tag{3}$$

where t is the time and $\bar{M}$ and $\bar{\gamma}$ are the average GB mobility and energy for the material. Here, we have approximated the change in the average curvature using the velocity of an average GB as defined by Eq. (1) with only the curvature driving force and no resistive forces. If we assume that the average GB mobility and energy are constant, we can then integrate Eq. (3) to obtain

$$\bar{D}^2 - \bar{D}_0^2 = 2\alpha \bar{M}\bar{\gamma}t, \tag{4}$$

where $\bar{D}_0$ is the initial average grain size. 3D grain growth simulations that only represent the curvature driving force produce

results in good agreement with this expression [15,16], as do experiments near the melting temperature [17].

In many polycrystal grain growth experiments, including both metals and ceramics, the grain growth is not accurately described by Eq. (4). Therefore, a semi-empirical equation is often used to describe the growth behavior, i.e.

$$\bar{D}^n - \bar{D}_0^n = Kt, \tag{5}$$

where the exponent n and the rate constant K are determined by fitting to experimental data. Values for the exponent n that best fit the data vary, ranging from 2 to 4 [17]. When $n = 2$, Eqs. (4) and (5) can be equated, giving $K = 2\alpha \bar{M}\bar{\gamma}$; however, this is not the case for any other value of n. The value of n has been shown to vary with porosity, impurities, residual stress, and more [17]. Equation (4) does not accurately describe the grain growth behavior in these cases because the assumptions used to derive the model are not true, i.e. that the curvature is the only significant driving force and that there are no significant resistive forces. For example, in a material with significant residual stress, the elastic and plastic driving forces would be significant in addition to the curvature; in a material with porosity or second phase particles, there would be significant resistive forces. It is important to note that when Eq. (5) is used with $n \neq 2$, the model is semi-empirical and it cannot be used to determine grain growth in a given material without data for fitting.

An alternative approach to modeling normal grain growth in materials with significant resistive force is to include the resistive force in Eq. (3), i.e.

$$\frac{\partial \bar{D}}{\partial t} = \alpha \bar{M}\bar{\gamma}\left(\frac{1}{\bar{D}} - \frac{\bar{P}}{\alpha^{1/2}\bar{\gamma}}\right), \tag{6}$$

where $\bar{P}$ is the average resistive force per unit area. Note that this equation still assumes that curvature is the only significant driving force. The resistive force can be estimated for second phase particles or porosity if the average radius of the porosity or second phase particles and the fraction of the GB area covered (the fractional coverage) are known [11]. The fractional coverage is difficult to obtain from experimental data; however, for any resistive pressure there will exist a maximum average grain size at which the driving force will equal the resistive pressure. This maximum grain size $\bar{D}_m = \bar{P}/\alpha^{1/2}\bar{\gamma}$, such that

$$\frac{\partial \bar{D}}{\partial t} = k\left(\frac{1}{\bar{D}} - \frac{1}{\bar{D}_m}\right), \tag{7}$$

where the rate constant $k = \alpha \bar{M}\bar{\gamma}$. Note that the rate constant k is twice the rate constant K used in Eq. (5) for cases with $n = 2$. Assuming $\bar{D}_m$ is constant, Eq. (7) can be integrated to give

$$\bar{D}_m(\bar{D}_0 - \bar{D}) + \bar{D}_m^2 \ln\left(\frac{\bar{D}_m - \bar{D}_0}{\bar{D}_m - D}\right) = kt. \tag{8}$$

However, if $\bar{D}_m$ is not constant (the average radius and/or fractional coverage of the porosity or second phase particles changes with time), the integral would need to be carried out numerically. This form simplifies the comparison with experimental data, as the maximum average grain size can often be estimated or fit.

Typical UO_2 grain growth experiments use sintered samples that are not fully dense. Therefore, there is porosity, and the resistive pressure is not zero. UO_2 grain growth data has most often been analyzed using Eq. (5), and the rate constant is defined with an Arrhenius expression as $K = K_0 \exp(-\frac{Q}{RT})$, where K_0 is the rate constant prefactor, Q is the activation energy, R is the ideal gas constant, and T is the temperature in K. Annealing data for unirradiated UO_2 have been used to determine values for n, K_0, and Q, with the exponent n ranging from 2.5 to 4.0 [6] for the various
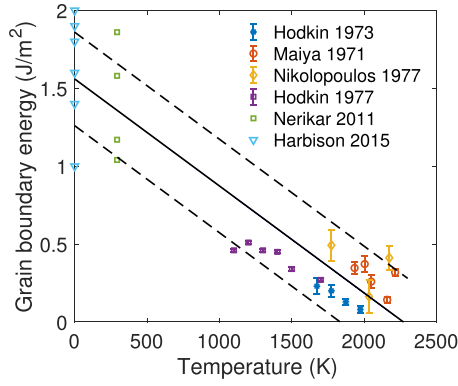
Fig. 1. GB energy values for UO$_2$ from measurements in the 1970s [19–22] and more recent MD simulations [23,24]. Note that the values shown from Ref. [24] are representative values from the hundreds of energies calculated. We also show a linear fit with temperature as a solid black line that we recommend as a reasonable value for the average UO$_2$ GB energy. The dashed lines show the uncertainty limits of the fit.

data. However, even when various data were fit with the same exponent n, the corresponding Q values varied by as much as 50%, and the K_0 values varied by as much as nine orders of magnitude. Only Ainscough et al. [5] have analyzed UO$_2$ grain growth data using Eq. (8). They fit values for $k = k_0 \exp(-\frac{Q}{RT})$ and $\bar{D}_m$. They also fit a value for $\bar{D}_m$ that decreases with increasing burnup for use with irradiated fuel. Their semi-empirical model is the most widely used to predict the change in UO$_2$ grain size in fuel performance codes [18].

3. Average GB energy and mobility in UO$_2$

Our new mechanistic model of grain growth in UO$_2$, like all mechanistic models, requires some estimate of the GB mobility and energy. While all of the mesoscale numerical simulation methods developed to model UO$_2$ have used GB mobility and energy values found in the literature, the selected values have varied widely. Therefore, we begin by surveying and discussing the various values available for the average GB energy and mobility for UO$_2$.

3.1. Grain boundary energy

The GB energy of UO$_2$ was measured using thermal groove experiments by various researchers in the 1970s [19–22], and the values are summarized in Fig. 1. These measurements targeted individual GBs arbitrarily selected from the surface, but their misorientations were not characterized. These GB energy values were fairly consistent, though they showed some scatter, possibly due to measurement error and variation in the misorientation of the selected GBs. They were also shown to vary with stoichiometry. All of the measured GB energy values decreased fairly linearly with temperature.

The energies of various UO$_2$ GBs have also been calculated with molecular dynamics (MD) simulations using the Basak potential [25] at room temperature [23] and at 0 K [24]. Nerikar et al. [23] selected four GBs found to be common in sintered UO$_2$ from electron backscatter diffraction data. Harbison [24] calculated the energies for hundreds of GBs in order to fit a continuous function to the data. The simulated values are much higher than the measured values, but when plotted with the experimental values, as done in Fig. 1, it is clear that they follow the same general trend with temperature.

For convenience in modeling, we have created a linear fit to the experimental data shown on Fig. 1 to obtain a value for the average GB energy $\bar{\gamma}$. The equation for the fit in terms of the temperature

T in K is

$$\bar{\gamma}(T) = (1.56 - 5.87 \times 10^{-4}T) \pm 0.3 \text{ J/m}^2, \tag{9}$$

where the uncertainty limits were set to encompass the majority of the experimental data. Our proposed fit corresponds well with the values calculated using the MD simulations. The reason for the linear dependence with temperature is unclear, though it could be due to entropy.

3.2. Grain boundary mobility

The GB mobility cannot be directly measured from experiments because it is always convoluted with the driving force. When only the curvature driving force is significant, the mobility is convoluted with the GB energy giving the reduced mobility $\bar{M} = \bar{\gamma}M$. The reduced mobility can be measured for individual GBs using bicrystal samples with specific geometries [26,27], but these approaches have never been applied to UO$_2$. Alternatively, polycrystalline samples can be annealed and the average grain size can be measured over time.

In order to extract the GB mobility from polycrystal measurements of the average grain size, the data must first be fit to a grain growth model such as Eq. (5) or Eq. (8). When the data is fit using Eq. (5), the rate constant K is sometimes converted to the GB mobility using the expression [28]:

$$\bar{M} = \frac{K}{n\bar{\gamma}\bar{D}^{n-2}}. \tag{10}$$

Thus, when the exponent $n = 2$, $\bar{M} = K/(2\bar{\gamma})$, which assumes that the geometric constant $\alpha = 1$. When the exponent $n > 2$, this expression results in a value for the GB mobility that depends on the average grain size. However, as we have established previously, the exponent $n > 2$ signifies that there are other driving forces and/or significant pinning forces present in the material. Thus, the mobility calculated using Eq. 10 for $n > 2$ is actually an effective mobility that also includes other effects.

When data is fit using Eq. (8), the rate constant can always be converted to the true mobility using the expression $\bar{M} = k/\bar{\gamma}$, assuming $\alpha = 1$. The actual value for the geometric constant α, which relates the average grain size with the average grain curvature, will vary depending on the shape of the grains and could vary between materials. Mesoscale simulations of GB migration in polycrystals using the phase field method (assuming isotropic GB properties) found $\alpha = 1/2$ in 2D simulations [9] and $\alpha = 1.0$ in 3D simulations [29]. More study is needed to determine the accuracy of the assumption that $\alpha = 1$.

We determine an expression for the average GB mobility for UO$_2$ from values for the rate constant k that were determined from multiple samples annealed at various temperatures by Ainscough et al. [5]. However, these rate constants were determined using average grain sizes that were measured using the linear intercept method without modification. The linear intercept $\bar{l}$ is not equivalent to the grain size; according to ASTM standard 112-13, the average grain size $\bar{D} = 1.571\bar{l}$. Thus, the linear intercept rate constants k from that work must be multiplied by the same factor to convert them to grain size rate constants. We have taken the rate constants from Ainscough et al. and converted them to grain size rate constants and then to mobilities using $\bar{M} = k/\bar{\gamma}$ with GB energies calculated from Eq. (9). We then fit an Arrhenius expression to the mobilities to determine values for M_0 and Q:

$$\bar{M} = M_0 \exp\left(-\frac{Q}{RT}\right). \tag{11}$$

In order to obtain reasonable fits for M_0 and Q, mobilities from multiple temperatures should be used. Ainscough et al. [5] determined rate constants for twelve batches of UO$_2$ samples, each with
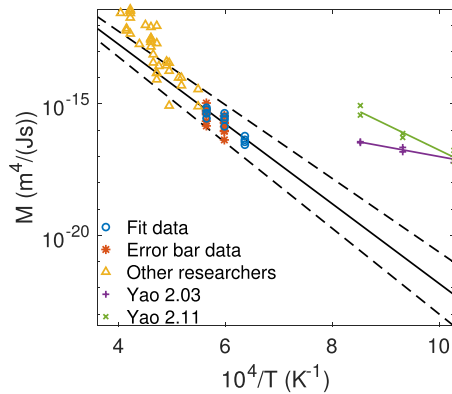
Fig. 2. Our fit of the average UO$_2$ GB mobility using data from Ainscough et al. [5]. The fit (solid black line) was determined from mobility values converted to rate constants for the four batches with values from three temperatures (labeled "Fit data"). The uncertainty limits (dashed black lines) were determined using data from the other eight batches (labeled "Error bar data"). Data from other researchers taken from Tab. 11 in Ref. [5] are shown for comparison. Data from Yao et al. [30] and the corresponding mobility fits are also shown.

different initial densities and grain sizes. Rate constants were obtained at three temperatures for four of the batches, but at only two temperatures for the other eight batches. We determined the values for our Arrhenius fit using the four batches with data for three temperatures. We then determined uncertainty limits on the fit values by comparing predictions to the data from the remaining eight batches. Our determined values are $M_0 = 2.14 \pm 0.15 \times 10^{-7}$ m^4/(Js) and $Q = 290 \pm 22$ kJ/mol $= 3.01 \pm 0.23$ eV. The mobility values, our Arrhenius fit, and the uncertainty are shown in Fig. 2. The fit is compared to data from five other researchers for which Ainscough et al. calculated rate constants, taken from Table 11 in Ref. [5]. The uncertainty limits of the fit encompass the majority of the data. All but one of the data points outside the uncertainty limits fall above the upper limit. Ainscough et al. suggest that these samples may be hyperstoichiometric due to issues with the methods used to control the stoichiometry.

A much more recent study from Yao et al. has investigated the grain growth in nanocrystalline UO$_2$ pellets that were fabricated using spark plasma sintering [30]. They focused on hyperstoichiometric samples, using samples of UO$_{2.03}$ and UO$_{2.11}$ with initial grain sizes ranging from 63 nm to 165 nm and porosities ranging from 1.3% to 4.0%. They annealed the samples at 700, 800, and 900 °C and ensured that the stoichiometry did not change during annealing. They analyzed the data by fitting a rate constant and grain size exponent, similar to Eq. 5, but they also fit an exponent on the time. Thus, their analysis cannot be directly compared with that from Ainscough et al. [5]. Therefore, we have reanalyzed the data here using Eq. (8) to calculate the mobility for UO$_{2.03}$ and UO$_{2.11}$, and the results and mobility fit are shown in Fig. 2. The mobilities (m^4/(Js)) are

$$\bar{M}_{2.03} = 5.00 \times 10^{-14} \exp\left(-\frac{0.73 \text{ eV}}{k_b T}\right), \tag{12}$$

$$\bar{M}_{2.11} = 1.18 \times 10^{-7} \exp\left(-\frac{1.95 \text{ eV}}{k_b T}\right). \tag{13}$$

These results show that the GB mobility increases with hyperstoichiometry, which has also been observed by other researchers. However, the activation energy for the mobility is much smaller than those obtained by our analysis and the analyses of other researchers using standard fuel pellets with larger grain sizes (0.73 eV and 1.95 eV versus 3.0 ± 0.21 eV). Yao et al. [30] hypothesize that the small activation energies are due to the small grain sizes. However, as mentioned previously, the GB mobility

should be independent of the grain size. An alternative explanation is that GB curvature is not the only significant driving force, e.g. there may be significant residual stress. If this is the case, then Eq. (8) cannot be used to determine the mobility.

MD simulations have also been used to calculate the GB mobility for UO$_2$. Bai et al. [31] calculated the GB mobility with MD using three different approaches. For all three approaches, the GB mobilities that were determined were many orders of magnitude higher than experimental values. These results illustrate a general issue with GB mobilities calculated using MD: MD calculates the intrinsic GB mobility for a perfect material without defects or impurities. Such defects in real materials have been shown to severely reduce the GB mobility [32].

Another approach used to determine the GB mobility is an analytical equation [28]:

$$\bar{M} = \frac{fD_b\Omega}{\delta_g RT}, \tag{14}$$

where D_b is the diffusion coefficient of the slower ion across the GB (the U ion in UO$_2$), f reflects the density of boundary core sites associated with high jump probabilities and is equal to one for high angle boundaries, Ω is the molar volume, and δ_g is the GB width. The diffusion coefficient D_b is typically assumed to be one or two orders of magnitude below the GB diffusion coefficient, though its actual value is rarely known. This is complicated in UO$_2$ because there is some discrepancy in the value of the diffusion coefficient for U ions along GBs; values measured in the 1960s are five orders of magnitude larger than values measured in 2000. This is likely due to issues in the measured bulk diffusion coefficient [33]. Eq. (14) has been used to calculate the GB mobility of UO$_2$ using a value for the U ion diffusion coefficient from the 1960s (reduced by one order of magnitude) [10], though the calculated value was roughly two orders of magnitude larger than the value from our fit using the data from Ainscough et al. [5]. We have recalculated the mobility using the smaller value from Ref. [33], giving a mobility that is three orders of magnitude smaller than our fit value. Thus, due to the large uncertainty in the value of D_b, this equation may not be an accurate means of determining the GB mobility in UO$_2$.

While Eq. 14 is not an accurate means of determining the GB mobility, it does provide important insights. In the equation, GB mobility is a linear function of the U ion GB diffusivity. Self diffusion is a linear function of the vacancy concentration for ions that diffuse via vacancy diffusion. Under thermal conditions, this makes the self diffusion a function of the vacancy equilibrium concentration and thus the formation energy of vacancies. However, in reactor conditions, the vacancy concentration will be elevated, accelerating self diffusion. Thus, the GB mobility may also be a linear function of the vacancy concentration and be elevated in reactor conditions.

4. Grain growth model with porosity

The objective of our new grain growth model is to predict the evolution of the average grain size at a specific material point of UO$_2$. The evolution should be a function of the temperature, the average GB energy and mobility of the material, as well as various types of porosity within the material. Thus, it must account for various physical phenomena, as summarized in the following subsections.

4.1. Model of the resistive force

The resistive force ($\bar{P}$ in Eq. (6)) of static particles/pores on GBs was first studied by Zener, assuming a single average particle/pore radius and randomly positioned particles/pores. It has since been

expanded to consider deviations from random positioning [34]. The average resistive force per unit area is

$$\bar{P} = \frac{3}{2} R \frac{\bar{\gamma} f_V}{r_p}, \tag{15}$$

where r_p is the particle/pore radius, f_V is the volume fraction of the particles/pores, and R is a stereological parameter that defines how many times more likely a particle/pore is to be found touching a GB than if they were randomly positioned. The determination of the resistive force is simplified if information is known directly about the particles/pores in contact with GBs [9]. If the fraction of the GB area covered by particles/pores f_c is known, then

$$\bar{P} = \frac{\bar{\gamma} f_c}{r_p}. \tag{16}$$

If the number of particles/pores per unit GB area N_p is known, then

$$\bar{P} = \bar{\gamma} \pi N_p r_p. \tag{17}$$

f_c and N_p are related according to $N_p = f_c/(\pi r_p^2)$. Note that these expressions assume that all of the particles/pores are spherical and the same size.

Due to variation in the pore size, the resistive force becomes a function of a random variable and will also vary. However, there are discrepancies in the literature regarding the impact of a particle/pore size distribution on the average resistive force. Researchers have used simulation and statistical analysis to investigate the impact of a size distribution, with one work indicating that it will increase the average resistive force [35] and another concluding that it will have no effect [36]. A third work predicted that the presence of a particle/pore size distribution will decrease the average resistive force [9], but this was due to an error in the statistical analysis.

The discrepancy is due, at least in part, to the assumptions regarding which parameters are treated as deterministic and which are treated as random variables. If the value of r_p varies but f_c and R are assumed to be constant (making N_p vary due to the variation of r_p), then Eq. (15) becomes a function of the expected or mean value $E(1/r_p)$ as follows:

$$\bar{P} = \frac{3}{2} R \bar{\gamma} f_V E\left(\frac{1}{r_p}\right). \tag{18}$$

The expected value of the inverse of a random variable tends to increase with the standard deviation of the random variable. Thus, in this case, the average resistive force would increase as the standard deviation of r_p increases. If r_p varies and f_c is assumed to not vary, then Eq. (16) also becomes a function of $E(1/r_p)$, and the resistive pressure will again increase as the standard deviation of r_p increases. However, if r_p varies and N_p is assumed to be constant (making f_c and f_V vary due to the variation of r_p), then Eq. (17) becomes a function of the expected or mean value of r_p, and the average resistive force will be constant as the standard deviation of r_p increases.

Porosity in UO_2 typically comes in the form of pores left over after sintering (typically defined by their volume fraction f_V) or in the form of fission gas bubbles (with their GB fractional coverage f_c predicted by a fission gas release model). Thus, Eqs. (15) and (16) are the most useful expressions for defining the pinning force in UO_2. Both sintered porosity and fission gas bubbles will always have a distribution of sizes. Therefore, it is important that we consider the impact of a size distribution on the pinning force. For that, we need to define the expected value of the inverse of the pore radius, as shown in Eq. (18). The expected value depends on the distribution of the pore radius, and in this work we will consider two distributions: uniform and lognormal. We will not consider a normal distribution because there is always some probability that normally distributed radii could take on negative values,
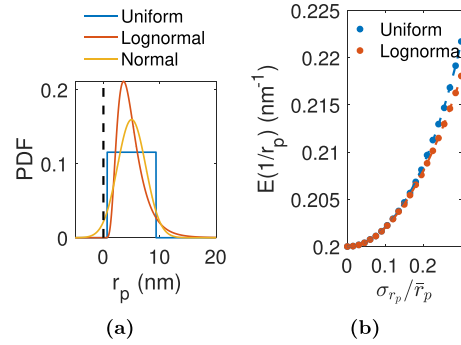
Fig. 3. Demonstration of the impact of a pore size distribution. (a) demonstrates that it is not possible to guarantee radii above zero when using a normal distribution by showing the probability density function (PDF) for a pore radius that follows a uniform, lognormal, and normal distribution. (b) compares the expected value of the inverse of the pore radius versus the ratio of the pore radius standard deviation to the mean from uniform and lognormal distributions. Both plots were made assuming an average pore radius $\bar{r}_p = 5$ nm.

which are non-physical, as illustrated in Fig. 3. The expected value of the inverse of the two distributions with a mean of $\bar{r}_p$ and a standard deviation σ_{r_p} are

$$E\left(\frac{1}{r_p}\right) = \frac{\ln r_{mx} - \ln r_{mn}}{r_{mx} - r_{mn}}, \tag{19}$$

for a uniform distribution, where $r_{mn} = \bar{r}_p - \sqrt{3}\sigma_{r_p}$ and $r_{mx} = \bar{r}_p + \sqrt{3}\sigma_{r_p}$, and

$$E\left(\frac{1}{r_p}\right) = e^{-\mu + \sigma/2}, \tag{20}$$

for a lognormal distribution, where $\mu = \ln(\bar{r}_p^2/\sqrt{\bar{r}_p^2 + \sigma_{r_p}^2})$ and $\sigma^2 = \ln(1 + \sigma_{r_p}^2/\bar{r}_p^2)$. The expected values from these two distributions for the inverse of a varying pore radius are compared for various standard deviations in Fig. 3.

4.2. Model of pore mobility

Pinning models predict that once the resistive force is equal to the driving force, GB motion stops. However, just as the particles/pores assert a resistive force on the GB, the GB also asserts an equivalent force on them. Thus, if they are mobile, such as in the case of pores, then the GB can drag them along at a velocity of

$$v_p = P \frac{M_p}{N_p}, \tag{21}$$

where N_p is the number of pores per unit GB area, and M_p is the pore mobility (with different units than the GB mobility) [28]. For spherical pores that migrate due to surface diffusion, the pore mobility is defined as

$$M_p = \frac{D_s \delta_s \Omega}{RT \pi r_p^4}, \tag{22}$$

where D_s is the surface diffusivity, and δ_s is the thickness of the surface layer. The expression changes for other migration mechanisms, but in all cases, it is a function of $1/r_p^n$, where $n = 4$ for surface diffusion, $n = 3$ for lattice diffusion, and $n = 2$ or 3 for vapor transport [28].

The expression for the pore mobility from Eq. (22) assumes that all pores are the same size. Therefore, we must modify Eq. (22) so that it accounts for a varying pore size. When we consider the pore radius as a random variable, the pore mobility M_p
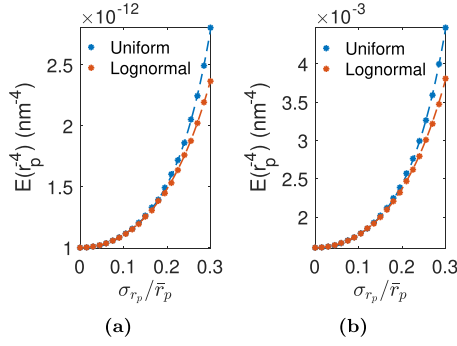
Fig. 4. The expected value $E(r_p^{-4})$ versus the ratio of the pore radius standard deviation to the mean for uniform and lognormal distributions, where (a) shows the values for the $\bar{r}_p = 1$ μm value used in the fit and (b) shows the values for $\bar{r}_p = 5$ nm. Note that the fit is accurate for both average radii.

becomes a random function that also follows a distribution. Its expected or mean value becomes

$$E(M_p) = \frac{D_s \delta_s \Omega}{RT\pi} E\left(r_p^{-4}\right). \tag{23}$$

Unfortunately, there is no closed form solution for the expected value of the inverse of random variable raised to the fourth power. Therefore, we have developed an empirical model of $E(r_p^{-4})$ by fitting to results from Monte Carlo simulations using a uniform and a lognormal distribution of the pore radii. We defined the empirical model as

$$E\left(r_p^{-4}\right) = \bar{r}_p^{-4} p_4\left(\frac{\bar{r}_p}{\sigma_{r_p}}\right), \tag{24}$$

where $p_4\left(\frac{\bar{r}_p}{\sigma_{r_p}}\right)$ is a fourth-order polynomial function of the mean bubble radius divided by its standard deviation. We fit the polynomial to five million values of r_p^{-4}, in which the values of r_p were sampled from the given distribution with $\bar{r}_p = 1$ μm and standard deviation values up to $\sigma_{r_p} = 0.3\bar{r}_p$. The fitted functions for the two distributions are

$$p_4^{uni} = 333.8a^4 - 109.9a^3 + 25.2a^2 - 0.7a + 1.0, \tag{25}$$

$$p_4^{logn} = 103.4a^4 - 21.9a^3 + 12.9a^2 - 0.1a + 1.0, \tag{26}$$

where p_4^{uni} and p_4^{logn} are the polynomial functions for the uniform and lognormal distributions, respectively, and $a = \bar{r}_p/\sigma_{r_p}$. Note that these fits are only valid for random pore radii that vary according to the specific distribution within the range of standard deviation values used for the fit. While the polynomials were fit using a specific average pore radius, they are valid for any average radius. Fig. 4 shows $E(r_p^{-4})$ from Monte Carlo simulations and calculated using Eq. (24) for the $\bar{r}_p = 1$ μm value used in the fit and for $\bar{r}_p = 5$ nm, and in both cases, the equation is quite accurate. It is also clear that $E(r_p^{-4})$ is sensitive to the standard deviation of the pore radius, with the sensitivity increasing with the value of the standard deviation.

As stated in the previous section, the impact of variation of the pore size on the expected value of the pinning force depends on whether f_c or N_p is considered to be deterministic. The same is true for the pore velocity. If we assume that N_p is deterministic, then f_c will vary, and the pore velocity becomes

$$v_p = P\frac{E(M_p)}{N_p}. \tag{27}$$

If we assume that the GB fractional coverage f_c is deterministic and the pore sizes vary, then N_p will also vary, and the pore velocity

becomes

$$v_p = PE(M_p)E\left(\frac{1}{N_p}\right), \tag{28}$$

where $E(1/N_p) = (\bar{r}_p^2 + \sigma_{r_p}^2)\pi/f_c$.

4.3. Model of grain growth with mobile pores

Recent simulations of GB pinning by mobile porosity have shown that GB and pore interactions are complicated [12]. If the velocity of a pore and GB are equal, then both move forward together and stay in contact. However, if the velocity of the GB is faster than the pore, then the GB will wrap around the pore and may eventually release from it. One approach to modeling GB motion in the presence of mobile pores is to use an effective mobility that includes contributions from the mobilities of the GBs and the pores [14]. This approach assumes that the velocities of GBs and pores are equal and

$$v_p = v_g,$$

$$\frac{M_p}{N_p}P_g = M_g(F_g - P_g),$$

$$P_g\left(\frac{M_p}{N_p} + M_g\right) = M_g F_g. \tag{29}$$

If we substitute in $P_g = v_p N_p/M_p$ and solve for v_g, we obtain

$$v_g = v_p = M_{eff} F_g, \tag{30}$$

where the effective mobility is given by

$$M_{eff} = \frac{M_g M_p}{M_p + N_p M_g}. \tag{31}$$

However, this approach forces the GBs and pores to have the same velocity and over-constrains the behavior when this is not the case.

We propose an alternative approach to modeling the GB velocity with mobile pores. In our new model, we begin with Eq. (1) but we consider mobile pores. In that case, the velocity from Eq. (1) becomes the relative velocity of the GB with respect to the pores. If we consider $P_g \le F_g$ and use Eq. (21) to define the velocity of a pore, this gives

$$v_g - v_p = M_g(F_g - P_g),$$

$$v_g = M_g(F_g - P_g) + \frac{M_p}{N_p}P_g. \tag{32}$$

We note that pores can slow a GB down, but they cannot speed one up. We therefore add the additional constraint

$$v_g = M_g F_g - \left[M_g P_g - \frac{M_p}{N_p}P_g\right]^+. \tag{33}$$

Depending on the relative values of the GB and pore mobilities, and of the driving and resistive forces, this model suggests four different regimes:

1. $M_g \le \frac{M_p}{N_p}$ Pores are more mobile than GBs and so they have no impact on the GB velocity, irrespective of the resistive force. The second term in Eq. (33) is then null, leading to $v_g = M_g F_g$.

2. $M_g \ge \frac{M_p}{N_p}$ and $P_g < F_g$ Pores are slower than GBs and their resistive force is not enough to cancel out the driving force. The GB velocity is impacted by both the pore and GB mobilities, as defined by Eq. (33), though the []$^+$ operator is not needed.

3. $M_g \gg \frac{M_p}{N_p}$ and $P_g < F_g$ The pores are effectively immobile. Equation (33) becomes Eq. (1).

4. $M_g \ge \frac{M_p}{N_p}$ and $P_g \ge F_g$ The resistive force cancels out the driving force, so that GBs and pores migrate at the pore velocity. Eq. (33) becomes equal to Eq. (21), such that $v_g = v_p = \frac{M_p}{N_p}F_g$.

Table 1
Properties for UO_2 needed to calculate the pore mobility. The value or expression for each property is provided, as well as the reference when applicable.

Property	Value	Reference
D_s	$D_{s0}e^{-\frac{E_m}{RT}}$	
D_{s0}	$54\,m^2/s$	[19]
E_m	$452\,kJ/mol$	[19]
δ_s	$0.5\,nm$	*assumed*
Ω	M/ρ	
M	$270.03\,g/mol$	
ρ	$10.97\,g/cm^3$	

In the new model, if the variation of the pore size is considered, the equation is essentially unchanged, except that we calculate the expected grain velocity and we use the expected value of P_g in the first term in the $[\,]^+$ operator, $M_g P_g$ (M_g is deterministic). The expected value of the second term in the $[\,]^+$ operator is given by

$$E\left(\frac{M_p}{N_p}P_g\right) = \frac{\gamma D_s \delta_s \Omega}{RT}E\left(r_p^{-3}\right). \tag{34}$$

The expected value $E\left(r_p^{-3}\right)$ also does not have a closed-form solution. We fit its value for the uniform and lognormal distributions in the same manner as was done for $E\left(r_p^{-4}\right)$, with $E\left(r_p^{-3}\right) = \bar{r}_p^{-3}p_3\left(\frac{\bar{r}_p}{\sigma_{r_p}}\right)$. The fitted values are given by

$$p_3^{uni} = 31.8a^3 - 1.9a^2 + 0.6a + 1.0, \tag{35}$$

$$p_3^{logn} = 10.9a^3 + 3.7a^2 + 0.2a + 1.0, \tag{36}$$

where $a = \bar{r}_p/\sigma_{r_p}$.

We demonstrate our model by calculating the velocity of a UO_2 GB with a radius of curvature of $7\,\mu m$ at 1200 K. We use the GB energy and mobility defined by Eqs. (9) and (11), respectively, and the properties required to calculate the pore mobility are shown in Table 1. We consider two cases, one (shown in Figs. 5a and 5 b) in which $f_c = 0.05$ and we vary the pore average radius from 1 to 1000 nm (N_p decreases as the radius increases), and one (shown in Figs. 5(b) and 5(d)) in which $N_p = 2.5 \times 10^{10}$ pores/m^2 and we vary the pore average radius from 1 to 2000 nm (f_c increases as the radius increases). We also calculate the velocity using the pinning model (Eq. (1)) and the effective mobility (Eq. (30)), for comparison.

The values of the average GB velocity for pore radii ranging from 1 to 1000 nm with the GB coverage f_c held constant are shown in Fig. 5a. The system is in Regime 1 for small values of the pore radius, as the mobility of small pores is very high. In Regime 1, our new model (Eq. (33)) predicts a velocity equal to the unimpeded GB velocity, since the pores are more mobile than the GB. The pinning model with static pores predicts that the GB is immobile (since P_g is a function of $1/r_p$, as shown in Eq. (16)), while the effective mobility predicts a velocity equal to the unimpeded velocity for the smallest pore but it decreases rapidly with increasing radius.

As the pore radius increases, $\frac{M_p}{N_p}$ decreases and becomes smaller than M_g for $r_p = 63$ nm, transitioning to Regime 4. In Regime 4, the new model predicts that the velocity rapidly decreases with increasing radius, and its prediction is roughly equivalent to the effective mobility. The pinning model still predicts that the GB is immobile.

Like M_p, P_g also decreases with increasing pore radius (though it changes with $1/r_p$ rather than $1/r_p^4$, like M_p); once $r_p > 350$ nm, $P_g < F_g$ and the system is in Regime 2. The new model predicts that the GB velocity now increases with increasing radius, due to the
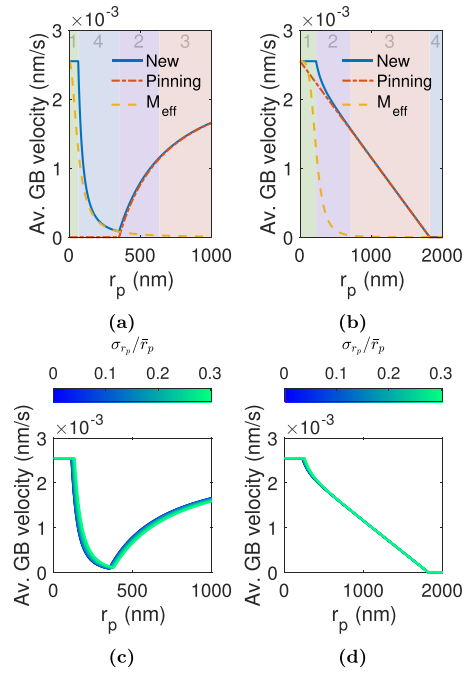
Fig. 5. The velocity of a UO_2 GB with a radius of curvature $R_g = 7\,\mu m$ predicted by our new model (Eq. (33)) for various pore radii. (a) and (b) compare the value from the new model with that predicted by the M_{eff} (Eq. (30)) and the pinning model with static particles (Eq. (1)). The different regimes are shaded and labeled, where light green indicates Regime 1, light purple indicates Regime 2, light orange indicates Regime 3, and light blue indicates Regime 4. (c) and (d) demonstrate the impact of a lognormal pore size distribution, where the line colors indicate the ratio of the pore radius standard deviation to its mean. The cases shown in (a) and (c) have $f_c = 0.05$ and the values of N_p changing with pore radius. The cases shown in (b) and (d) have $N_p = 2.5 \times 10^{10}$ pores/m^2 and the value of f_c changing with radius. (For interpretation of the references to colour in this figure legend, the reader is referred to the web version of this article.)

decrease in P_g. The pinning model also predicts an increasing GB velocity with increasing radius, and its predicted velocity is slightly slower than that from the new model. The effective mobility predicts that the velocity continues to decrease with increasing radius.

As both M_p and P_g continue to decrease, the pores become effectively immobile and the system enters Regime 3 around $r_p = 640$ nm. The new model and the pinning model predictions are identical, predicting that the GB velocity increases with increasing pore radius, but at a decreasing rate. The velocity from the effective mobility is essentially zero.

GBs impeded by mobile pores should move at velocities equal to or faster than GBs impeded by immobile particles/pores. Our new model predicts velocities much faster than the pinning model in Regimes 1 and 4, slightly faster than the pinning model in Regime 2, and equal to the pinning model in Regime 3. The effective mobility also predicts GB velocities that are faster than the pinning model in Regimes 1 and 4, but it predicts velocities that are much slower than the pinning model in Regimes 2 and 3.

The values of average GB velocity for pore radii ranging from 1 to 2000 nm when the number of pores per unit GB area N_p is held constant are shown in Fig. 5b. The system is again in Regime 1 for small values of the pore radius, and our new model again predicts a velocity equal to the unimpeded GB velocity. With N_p constant, the pinning model predicts the unimpeded GB velocity for $r_p = 1$ nm, and it decreases linearly with r_p, since P_g is now a linear function of r_p, as shown in Eq. (17). The effective mobility predicts a velocity higher than the pinning model for very small pore radii, but its velocity decreases quickly with increasing pore radius and drops below the pinning model.

The pore velocity decreases rapidly with increasing pore radius, and the system enters Regime 2 as M_p/N_p decreases and becomes smaller than M_g at $r_p = 225$ nm. In Regime 2, our new model decreases rapidly with increasing radius and approaches the velocity predicted by the pinning model. The effective mobility predicts a GB velocity that is much lower than the pinning model.

When $r_p > 710$ nm, the pores are effectively immobile. Here, the system enters Regime 3, in which the new and pinning models are equivalent. The velocity from the effective mobility is effectively zero for all $r_p > 710$ nm.

At $r_p = 1818$ nm, the system enters Regime 4 with $F_g = P_g$ and $M_p \approx 0$, such that all three models predict that the GBs are immobile.

From the results of these two cases, it is clear that our new model accounts for the correct physics in each of the four regimes. The pinning model tends to under-predict the GB velocity in regimes 1, 2, and 4, since it assumes immobile pores. The effective mobility tends to under-predict the GB velocity in regimes 1, 2, and 3, since it forces the GB and pore velocities to be equal.

The impact of variation in the pore size differs between the two cases because the pore radius standard deviation affects P_g differently in each. We demonstrate the impact of variation in the pore size by modeling the same two cases but now allowing the pore size to vary according to a lognormal distribution. The simulations are repeated for values of the ratio of the pore radius standard deviation to its mean ranging from 0 to 0.3.

When f_c is held constant (Fig. 5(b)), both P_g and M_p increase as the standard deviation increases. The standard deviation has no impact on the GB velocity in Regime 1, because the pores are too mobile to impact the GB migration. In Regime 4, the GB velocity increases as the standard deviation increases for a given average pore radius, since the velocity is dominated by the pore mobility. The GB velocity decreases as the standard deviation increases for a given average pore radius in Regimes 2 and 3, since the velocity is dominated by the resistive force. The radii at which the system transitions between the various regimes increases as the standard deviation increases.

When N_p is held constant (Fig. 5), only M_p increases as the standard deviation increases, and P_g is independent of the standard deviation. Again, the GB velocity is independent of the standard deviation in Regime 1. In Regime 2, the velocity increases with increasing standard deviation due to the increase in M_p. The velocity is unchanged by the standard deviation in Regimes 3 and 4. The radius at which the system transitions between Regimes 1 and 2 increases as the standard deviation increases, but all the other transitions are independent of the standard deviation.

While the impact of variation in the pore size on the GB velocity is significant, as illustrated by Figs. 5(b) and 5(d), it is small compared to the impact of the pore radius. A pore size distribution will not result in large changes to the grain growth of a material.

Equation (33) describes the velocity of a specific GB. If we consider a polycrystal with average grain size $\bar{D}$ with only the curvature driving force, as we did to develop Eq. (3), but we let the change in the average velocity be described by Eq. (33), we obtain:

$$\frac{\partial \bar{D}}{\partial t} = \alpha \bar{M} \frac{\bar{\gamma}}{\bar{D}} - \alpha^{\frac{1}{2}} \left[\bar{M}\bar{P} - \frac{M_p}{N_g}\bar{P} \right]^{+}. \tag{37}$$

Given the initial average grain size $\bar{D}_0$, this equation can be solved numerically to determine the average grain size as a function of time. It can be applied to any material with pores resisting grain growth for which curvature is the only significant driving force and for which the pore mobility and the GB mobility and energy are known.

4.4. Grain growth model for UO$_2$

The new mechanistic grain growth model must predict the change in the average grain size of UO$_2$ as a function of temperature, the sintered porosity p and their average radius, and the fission gas bubbles defined by the fraction of GBs covered by fission gas f_c and their average radius. These variables describing the average state of the fuel microstructure at a given material point would be calculated by a densification model for p and a fission gas release model for f_c. The model from Eq. (37) defines the change in the average grain size in a microstructure with pores, but it only considers one type of pore. The model needs to be expanded to consider the impact of two types of pores, namely the sintered pores and the fission gas bubbles.

If both types of porosity are more mobile than the GBs, then the pores have no impact on the grain growth. If only one type of porosity is more mobile than the GBs, then the other impacts the change in the average grain size with time according to Eq. (37). If both types of porosity are less mobile than the GBs, then both types of porosity will impact the grain growth. If the sum of the two resistive pressures is greater than or equal to the driving force, then the GBs are fully pinned and they move with the mobility of the pores. However, since the mobility of the two types of pores will vary, we use an effective pore mobility, such that

$$\frac{\partial \bar{D}}{\partial t} = \alpha M_{p,eff} \frac{\bar{\gamma}}{\bar{D}}. \tag{38}$$

The effective pore mobility is given by

$$M_{p,eff} = \frac{\sum_i f_{c,i} M_{p,i}/N_{p,i}}{\sum_i f_{c,i}}, \tag{39}$$

where $f_{c,i}$, $M_{p,i}$, and $N_{p,i}$ are the fractional coverage, pore mobility, and number of pores per unit GB area of the porosity type i, respectively. If the GBs are not fully pinned, the average grain size changes according to

$$\frac{\partial \bar{D}}{\partial t} = \alpha \bar{M} \frac{\bar{\gamma}}{\bar{D}} - \alpha^{\frac{1}{2}} \sum_p \left[\bar{M}\bar{P}_i - \frac{M_{p,i}}{N_{p,i}}\bar{P}_i \right]^{+}, \tag{40}$$

where $\bar{P}_i$ is the average resistive force of porosity type i, and the sum is taken over the two types of porosity: sintered pores and fission gas bubbles.
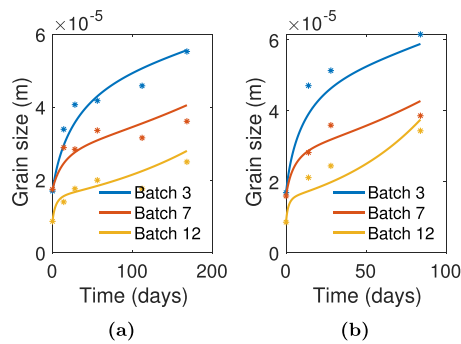
5. Model validation

We have validated the mechanistic grain growth model presented in the previous section using two validation cases, one on unirradiated UO$_2$ and one on irradiated UO$_2$.

5.1. Grain growth in unirradiated UO$_2$

For the first validation case, we compared against grain growth data in unirradiated UO$_2$ samples from Ainscough et al. [5]. As discussed above, these samples have porosity left over from sintering that resist grain growth and can be accounted for with our new model. While Ainscough et al. provide grain growth data from twelve different batches, we selected three to compare against: Batches 3, 7, and 12. We selected these batches because they are the only batches with data quantifying the densification of the fuel during the experiment, though only the initial and final densities are provided. The authors state that the densification is not linear and that in many cases it ceased after the first third of the annealing time, but no specific information is given about the individual batches. Also, no information was provided regarding the sizes of the pores.

We applied our model to simulate the increase in the average grain size of Batches 3, 7, and 12 at 1400 °C and 1500 °C using

Fig. 6. Validation of our new grain growth model by comparing to grain growth data for unirradiated UO$_2$ [5]. Specifically, we compare against data from Batches 3, 7, and 12. The average pore radii were fit using the data at 1400 °C, shown in (a), and we validated the model using the data at 1500 °C, shown in (b).

the properties from Table 1 as well as the GB energy and mobility from Eqs. (9) and (11). We assumed that the pore volume fraction decreased due to densification according to $\dot{f}_V = -Af_V^{1/3}$, as suggested by the model from Kang et al. [37]. We determined the value for A using the given initial and final relative densities. We also assumed that the average pore radius was different in the different batches, and that the pore radii followed a lognormal distribution with a standard deviation $\sigma_{r_p} = 0.2\bar{r}_p$. We fitted the values of the average radii by minimizing the error for the 1400 °C case and used the 1500 °C case for validation. The fitted $\bar{r}_p$ were 7.5 μm for Batch 3, 4.3 μm for Batch 7, and 2.3 μm for Batch 12. Note that the fit values for the average pore radii increased with average grain size.

The predicted average grain sizes at 1400 °C after fitting $\bar{r}_p$, as well as the experimental data, are shown in Fig. 6. The predicted average grain sizes and the experimental data at 1500 °C are shown in Fig. 6, and they compare reasonably well with the experimental data. For Batch 3, the predicted average grain sizes are somewhat below the experimental grain sizes; for Batch 7, they compare well; for Batch 12, they are below the experimental grain sizes initially but the final average grain size is slightly above the experimental value. Thus, the model performs well for fresh fuel. Note that the pore mobility is negligible for these cases due to the large average pore radii, such that the growth is only a function of the GB energy and mobility, and the pinning force.

5.2. Grain growth in irradiated UO$_2$

Next, we validated against grain growth data from irradiated fuel. In irradiated fuel, the porosity left over from sintering resists grain growth. However, the volume fraction of sintered porosity decreases with time due to irradiation-enhanced densification. In addition, gaseous fission products segregate to GBs and form bubbles that resist grain growth. Ainscough et al. [5] provide grain growth data from two irradiated fuel pellets, each irradiated at a different power and for a different time. Little information is given about how the data were collected, but it appears that the average grain size was measured at various locations across the radius of the pellets during post-irradiation examination. These average grain sizes were then correlated with corresponding irradiation temperatures, which must have been calculated using a model, since the capability to measure the temperature at multiple locations across the radius of a fuel pellet within a reactor was not available in 1973 (and would be difficult even today). The final burnups of the specimens were given, but no data regarding their sintered porosity or the fission gas bubble contents were provided.

Since these data do not provide any information regarding the porosity in the fuel microstructure, we cannot use our new model to predict the grain growth and directly compare it with the

data. However, Ainscough et al. used these data to fit a burnup-dependent empirical model for the maximum grain size from Eq. (6). This empirical grain growth model is currently used in the BISON fuel performance code [38], along with an empirical densification model that decreases the sintered porosity over time, and a fission gas release model that evolves descriptions of the GB fission gas bubbles. These models in BISON provide a means of estimating the porosity evolution within irradiated fuel and the prediction of the empirical grain growth model can be used as a rough surrogate for experimental data. Thus, we used values of the temperature, sintered porosity behavior, and fission gas bubble behavior outputted from BISON simulations in our model and predicted the increase in the average grain size. We then compared these predictions against the empirical grain growth model developed by Ainscough et al. [5].

We ran two BISON simulations and outputted the temperature, volume fraction of sintered porosity, GB fractional coverage by fission gas bubbles, and average GB bubble radius at various locations. The BISON simulations predicted the fuel performance of a smeared ten pellet rodlet in axisymmetric coordinates (as described in Ref. [38] and using a standard example input file). One simulation was carried out at a linear power of 29 kW/m for 830 days and the other at a linear power of 37 kW/m for 320 days. For each, the values were outputted at the pellet center ($r = 0$ mm), at an intermediate radius ($r = 2.3$ mm), and near the outer radius ($r = 4.5$ mm). The 29 kW/m and 37 kW/m cases were conducted with initial average grain sizes of 8 μm and 12 μm, respectively. The densification model in BISON does not determine the average radius of the sintered porosity, so we used the fitted value of 2.3 μm from the previous example from the batch with the closest initial grain size (Batch 3). We also assumed that the size of all porosity varied according to a lognormal distribution with $\sigma_{r_p} = 0.2\bar{r}_p$. We calculated the average grain size over time using our new model and compared its predictions with those from the empirical grain growth model from Ref. [5]. We used the properties from Table 1 and Eqs. (9) and (11).

When we used all the values from Table 1 in our model, it predicted much less grain growth than the empirical model, as shown in Fig. 7. Both the models predict no grain growth at the outer edge of the fuel ($r = 4.5$ mm). At mid-radius ($r = 2.3$ mm), the empirical model predicted significant growth starting halfway through the irradiation time for both powers, but the new model predicted no growth for the 29 kW/m case and small initial growth for the 37 kW/m case. At the pellet center ($r = 0.0$ mm), the empirical model predicted rapid initial growth, then a region of no growth, and then a long region of linear growth while the new model only predicted rapid initial growth and no additional growth. One likely reason for this discrepancy is inaccuracy in the surface diffusivity. We obtained the activation energy E_m and prefactor D_{s0} for the surface diffusivity from Maiya [19], and in that work, they report an uncertainty of 10% to 15% on the activation energy. In addition, it is well known that the high concentration of vacancies that occurs during irradiation will accelerate diffusion.

To improve the performance of the model, we calibrated the value of the activation energy for surface diffusion using the 29 kW/m case. We found that a value of $E_m = 389$ kJ/mol gave the best performance, a 13.9% variation from the value reported by Maiya [19] and within the reported 10% to 15% uncertainty. The simulation predictions using the calibrated activation energy are shown in Fig. 7. After calibration against the 29 kW/m case, our new model predicted grain growth very similar to that from the empirical model. However, the final grain size is under-predicted at mid-radius and the grain size in the first half of the irradiation at the center is over-predicted. Using the calibrated value with the 37 kW/m case, the new model over-predicted the grain size at both mid-radius and at the pellet center, though the general trends are
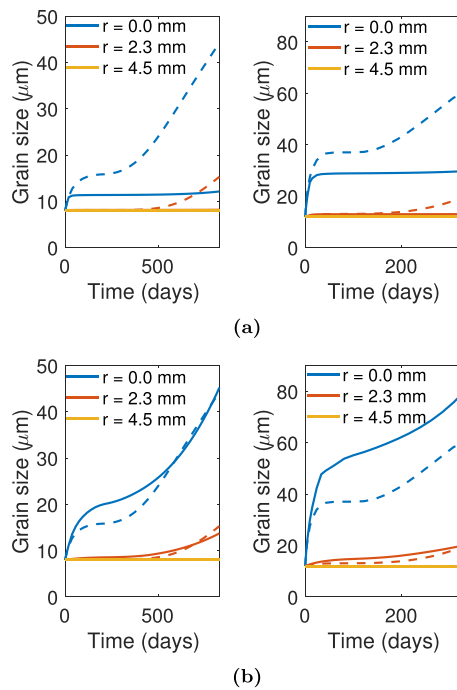
Fig. 7. Comparison of the grain sizes from our grain growth model to those predicted by the empirical model using values taken from BISON simulations. Results using a linear power of 29 kW/m are on the left and using a linear power of 37 kW/m are on the right. (a) shows the results using the published surface diffusion activation energy, and (b) shows the results using the activation energy that was calibrated using the 29 kW/m result. In each figure, solid lines show results from our new model, and dashed lines show results from the empirical model [5].

captured. At mid-radius, the final grain sizes compared very well. At the pellet center, our new model over-predicted the final grain size.

Though this validation is far from ideal because we are using descriptions of the porosity from models in BISON and we are comparing the grain sizes to an empirical model rather than experimental data, the comparison is reasonable for the 37 kW/m case, for which no calibration was carried out. Thus, we now have a mechanistic model that predicts the change in the average grain size as a function of the temperature and porosity in the fuel. It can also be applied to other reactor fuels, as long as curvature is the only significant driving force, and the fission gas bubble mobility and GB mobility and energy are known.

6. Impact on fuel performance simulations

Having validated the model against experimental sintering data and an empirical grain growth model, we now show its impact on the results of fuel performance simulations. Our mechanistic grain growth model has been implemented in the BISON fuel performance tool [38]. It includes the impact of sintered porosity that decreases due to densification and fission gas bubbles that increase during reactor operation in the same manner as was done in Section 5.2. However, now the grain growth model is fully integrated into the BISON simulation, and the evolving grain size at every integration point in the mesh directly impacts the fission gas release model as part of the mechanistic set of materials models [39].

To demonstrate the performance of the new grain growth model in BISON, we incorporated it into one of the BISON assessment cases: Rod TSQ002 from the US PWR 16 × 16 assessment [40]. However, in the standard assessment case the power was low enough that the fuel temperature never exceeded 1250 K and very little grain growth would have occurred. To provide cases that

clearly demonstrate the capabilities of our new model, we changed the average linear heat rate to result in higher temperatures and substantial grain growth. We modeled two modified versions of the assessment. In the first, the average linear heat rate is constant with time; in the second, the relative changes with time in the average linear heat rate are unchanged from the original assessment but its magnitude is increased. These changes to the average linear heat rate make it impossible to make comparisons to other published results for this assessment case, but they provide a useful means of assessing the impact of our new grain growth model on the overall fuel performance, as compared to BISON simulations using the empirical model from Ainscough et al. [5]. In particular, the transient power case emphasizes the importance of including the impact of temperature and power history on grain growth, which is included in mechanistic models, like our new model, but not in empirical models. The fuel had an initial grain size of 17.6 μm. The simulations used the fitted value for E_m, the other values from Table 1, and Eqs. (9) and (11).

We first discuss the results from the simulations with constant power. The average linear heat rate used in the simulations is shown in Fig. 8(a). The average grain size was outputted at an axial position approximately halfway up the rod (2 m) at three radial locations ($r = 0$ mm, 2 mm, and 4 mm). The temperatures at those locations are shown in Fig. 8, and the grain sizes are shown in Fig. 8.

The temperature at the outer edge of the fuel pellet was cool enough that no grain growth occurred. At mid-radius (2 mm), our new grain growth model predicted significant grain growth starting after 2.5 years, reaching a final grain size of 20.4 μm after 4.5 years. The empirical model did not predict any significant grain growth until 4.0 years. However, once it started, it was much faster than predicted by the new model and the final grain size was 19.6 μm. At the center of the pellet, our new grain growth model again predicted the start of grain growth much earlier than the empirical model, but the final grain size predicted by the two models was quite similar (39.8 μm from our new model and 41.3 μm from the empirical model). After about 4 years, the predicted grain growth at the pellet center from the two models converged and from then on they were nearly identical.

A sensitivity study carried out on the fission gas release model in BISON [2] showed that the predicted fission gas release is somewhat sensitive to grain size, while the predicted gaseous swelling is highly sensitive to grain size. Therefore, we compare the fractional fission gas release and the gaseous swelling in the two simulations. The fission gas release fraction is shown in Fig. 8. While there is some deviation between the two simulations, especially at around 3 years, it is not large, and after 4.5 years there is almost no deviation. This indicates that the differences in the predicted grain size do not have a significant impact on the fission gas release. We see a similar trend in the gaseous swelling, shown in Fig. 8. There is almost no deviation at the pellet edge and mid-radius, though at the pellet center the swelling is slightly larger in the simulation using our new model after about 3 years.

The average linear heat rate used for the transient case is shown in Fig. 8(b), and the resultant temperatures at the same radial locations used for the constant power case are shown in Fig. 8. For this case, the new grain growth model predicted significantly more grain growth at mid-radius and at the center of the fuel pellet than the empirical model. However, the empirical model was fit to constant power data and is independent of the temperature history of the material, i.e. it will predict the same change in grain size at a given temperature and burnup whether the material was at a higher temperature previously or whether the temperature has been constant. In reality, the temperature history will impact the evolution of the sintered porosity and fission gas bubbles in the material and therefore will impact grain growth. The grain
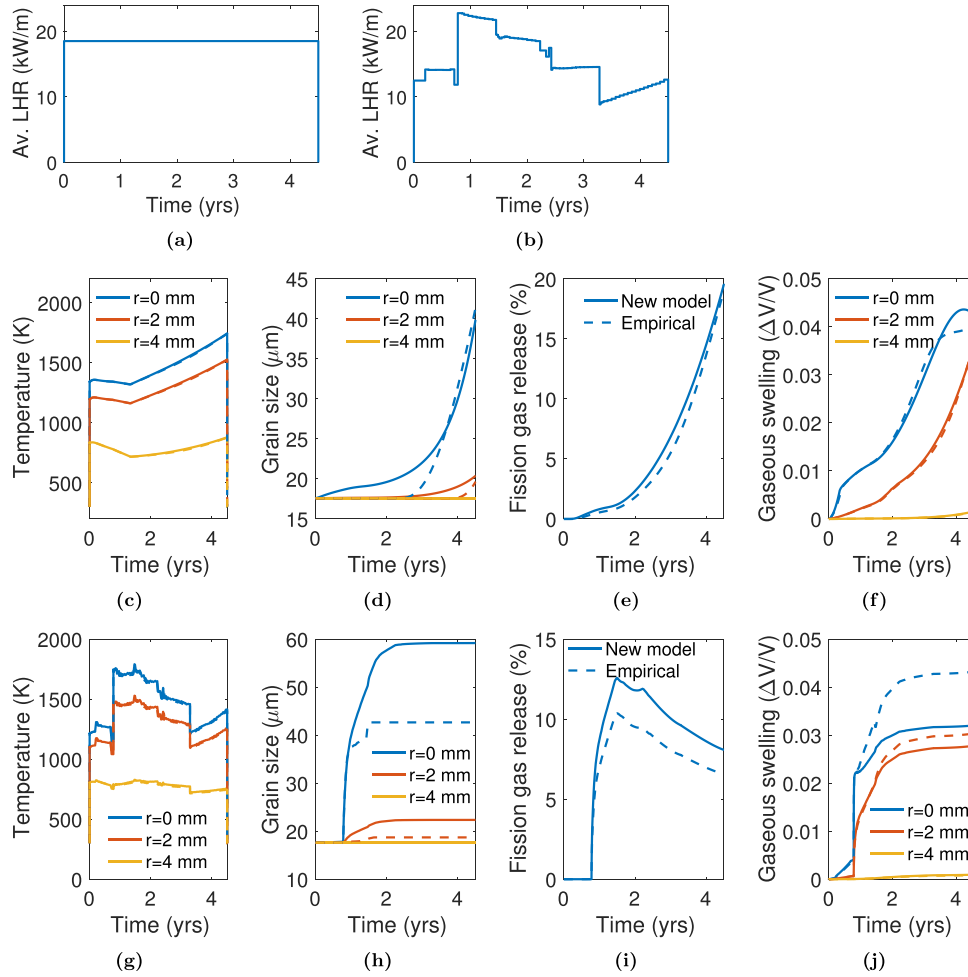
Fig. 8. Impact of our grain growth model on fuel performance simulations using BISON for constant and transient power cases. (a) and (b) show the average linear heat rates for the two cases. (c) - (f) show results for the constant power case, and (g) - (j) show results for the transient power case. (c) and (g) show the pellet temperature with time at three radial locations at an axial location of 2 m (approximately mid-rod), (d) and (h) show the grain size with time at the same radial and axial locations, (e) and (i) show the fractional fission gas release with time, and (f) and (j) show the gaseous swelling at the same locations. In each figure, solid lines show results obtained using the new grain growth model and dashed lines show results obtained using the empirical model from Ainscough et al. [5].

growth predicted by our new mechanistic model is directly a function of the evolution predicted by the densification and fission gas release models and therefore does account for this history effect. It predicts more grain growth than the empirical model because the high temperatures in the first few years of the irradiation reduced the resistive force due to the bubbles and porosity.

The significant grain growth that occurs during the high temperature transients in this case results in an increase in fission gas release and a decrease in gaseous swelling, as compared to the results with the empirical model. The increase in fission gas release begins at the start of the first transient (after 1 year), and the fractional release in the simulations using our new model is higher than that using the empirical model for the rest of the simulation (with a final difference of 20%). Note that the fractional release decreases after about two years because as the temperature decreases, fission gas diffusion is slowing at a much higher rate than the decrease in gas production, trapping more gas within the fuel. The gaseous swelling at the outer radius of the pellet is the same in both simulations; at the mid-radius, the simulation using our new model results in less swelling than that using the empirical model after about two years with a final difference of about 10%. At the pellet center, the simulation using our new model results in less swelling starting after about one year, with a final difference of 35%. It is important to note that the fission gas release model in BISON [1] is a mechanistic model and does correctly consider the

impact of the temperature and power history; therefore, these differences fully result from our new grain growth model. Thus, the fact that the empirical grain growth model does not consider the impact of power transients can significantly increase the error in the prediction of fission gas release and gaseous swelling.

7. Conclusions

We have developed a mechanistic grain growth model for UO_2 that accounts for pinning by porosity left over from sintering and by fission gas bubbles, and that accounts for dragging of porosity by GBs. In support of the model, we have created a new fit (including uncertainty limits) of existing experimental data to obtain the average GB energy as a linear function of temperature, which is also consistent with atomistic simulation results. We used this fit along with data presented in Ainscough et al. [5] to create a new fit of the average GB mobility and its associated uncertainty limits. Our results indicate that recent data from nanoscrystalline UO_2 samples [30] likely have an additional driving force, such as residual stress, that causes them to differ from the older data.

We have presented a model of the resistive force due to particles/pores that considers either a uniform or lognormal particle/pore size distribution. We have also developed a model of the pore mobility that considers a pore size distribution. We then developed a model of grain growth with mobile pores and com-

pared its predictions to the classical pinning and effective mobility models. Our new model that considers mobile pores accurately describes the behavior of four different regimes related to the relationships between the GB and pore mobilities and the driving and resistive forces. The pinning and effective mobility models each only accurately describe the GB velocity for one of the four regimes. We then expanded the model to include two distributions of porosity: sintered porosity and fission gas bubbles. The model was then calibrated to and validated against grain growth data for unirradiated UO_2 and the empirical grain growth model for irradiated UO_2 from Ainscough et al. [5]. Finally, we demonstrated the impact of our new mechanistic model on fuel performance simulations using the BISON tool for constant and transient power cases. Our model predicts similar results to the empirical model for the constant power case. However, since the new mechanistic model accounts for the impact of the temperature and power history on fuel microstructure, it predicts significantly more grain growth for the transient power case. While the mechanistic model was presented here for UO_2, it could be used for other fuels in which curvature is the only significant driving force, as long as the pore mobility and GB mobility and energy are known or can be estimated.

Declaration of Competing Interest

All authors have participated in (a) conception and design, or analysis and interpretation of the data; (b) drafting the article or revising it critically for important intellectual content; and (c) approval of the final version.

This manuscript has not been submitted to, nor is under review at, another journal or other publishing venue.

The authors have no affiliation with any organization with a direct or indirect financial interest in the subject matter discussed in the manuscript.

Acknowledgements

References

[1] G. Pastore, L. Luzzi, V. Di Marcello, P. Van Uffelen, Physics-based modelling of fission gas swelling and release in UO_2 applied to integral fuel rod analysis, Nucl. Eng. Des. 256 (2013) 75–86.

[2] G. Pastore, L. Swiler, J.D. Hales, S.R. Novascone, D.M. Perez, B.W. Spencer, L. Luzzi, P. Van Uffelen, R.L. Williamson, Uncertainty and sensitivity analysis of fission gas behavior in engineering-scale fuel modeling, J. Nucl. Mater. 456 (2015) 398–408.

[3] M. Oguma, Microstructure effects on fracture strength of UO_2 fuel pellets, J Nucl Sci Technol 19 (12) (1982) 1005–1014.

[4] K. Shrestha, T. Yao, J. Lian, D. Antonio, M. Sessim, M. Tonks, K. Gofryk, The grain-size effect on thermal conductivity of uranium dioxide, J Appl Phys 126 (12) (2019) 125116.

[5] J.B. Ainscough, B.W. Oldfield, J.O. Ware, Isothermal grain growth kinetics in sintered UO_2 pellets, J. Nucl. Mater. 49 (2) (1973) 117–128, doi:10.1016/0022-3115(73)90001-9.

[6] L. Bourgeois, P. Dehaudt, C. Lemaignan, J.P. Fredric, Pore migration in UO_2 and grain growth kinetics, J. Nucl. Mater. 295 (1) (2001) 73–82, doi:10.1016/S0022-3115(01)00502-5.

[7] O.V. Khoruzhii, S.Y. Kourtchatov, V.V. Likhanskii, New model of equiaxed grain growth in irradiated UO_2, J. Nucl. Mater. 265 (1) (1999) 112–116, doi:10.1016/S0022-3115(98)00632-1.

[8] H. Hallberg, Y. Zhu, Stability of grain boundary texture during isothermal grain growth in UO_2 considering anisotropic grain boundary properties, J. Nucl. Mater. 465 (2015) 664–673, doi:10.1016/j.jnucmat.2015.06.052.

[9] M.R. Tonks, Y. Zhang, X. Bai, P.C. Millett, Demonstrating the temperature gradient impact on grain growth in UO_2 using the phase field method, Materials Research Letters 2 (1) (2014) 23–28, doi:10.1080/21663831.2013.849300.

[10] K. Ahmed, J. Pakarinen, T. Allen, A. El-Azab, Phase field simulation of grain growth in porous uranium dioxide, J. Nucl. Mater. 446 (1–3) (2014) 90–99, doi:10.1016/j.jnucmat.2013.11.036.

[11] M.R. Tonks, Y. Zhang, A. Butterfield, X.-M. Bai, Development of a grain boundary pinning model that considers particle size distribution using the phase field method, Modelling Simul. Mater. Sci. Eng. 23 (4) (2015) 045009, doi:10.1088/0965-0393/23/4/045009.

[12] K. Ahmed, M. Tonks, Y. Zhang, B. Biner, A. El-Azab, Particle-grain boundary interactions: a phase field study, Comput. Mater. Sci 134 (2017) 25–37, doi:10.1016/j.commatsci.2017.03.025.

[13] Y. Guo, Z. Liu, Q. Huang, C.-T. Lin, S. Du, Abnormal grain growth of UO_2 with pores in the final stage of sintering: a phase field study, Comput. Mater. Sci 145 (2018) 24–34, doi:10.1016/j.commatsci.2017.12.057.

[14] M.N. Rahaman, Ceramic processing and sintering, CRC press, 2003.

[15] C.E. Krill III, L.Q. Chen, Computer simulation of 3-D grain growth using a phase-field model, Acta Mater 50 (12) (2002) 3059–3075, doi:10.1016/S1359-6454(02)00084-8.

[16] Q. Yu, S.K. Esche, Three-dimensional grain growth modeling with a monte carlo algorithm, Mater Lett 57 (30) (2003) 4622–4626, doi:10.1016/S0167-577X(03)00372-0.

[17] H. Hu, B.B. Rath, On the time exponent in isothermal grain growth, MT 1 (11) (1970) 3181–3184, doi:10.1007/BF03038435.

[18] P.V. Uffelen, R.J. Konings, C. Vitanza, J. Tulenko, Analysis of reactor fuel rod behavior, Handbook of nuclear engineering (2010) 1519–1627.

[19] P.S. Maiya, Surface diffusion, surface free energy, and grain-boundary free energy of uranium dioxide, J. Nucl. Mater. 40 (1) (1971) 57–65, doi:10.1016/0022-3115(71)90116-4.

[20] E.N. Hodkin, M.G. Nicholas, Surface and interfacial properties of stoichiometric uranium dioxide, J. Nucl. Mater. 47 (1) (1973) 23–30, doi:10.1016/0022-3115(73)90182-7.

[21] E.N. Hodkin, M.G. Nicholas, Surface and interfacial properties of non-stoichiometric uranium dioxide, J. Nucl. Mater. 67 (1) (1977) 171–180, doi:10.1016/0022-3115(77)90172-6.

[22] P. Nikolopoulos, S. Nazar, F. Thmmler, Surface, grain boundary and interfacial energies in UO_2 and UO_2-Ni, J. Nucl. Mater. 71 (1) (1977) 89–94, doi:10.1016/0022-3115(77)90191-X.

[23] P.V. Nerikar, K. Rudman, T.G. Desai, D. Byler, C. Unal, K.J. McClellan, S.R. Phillpot, S.B. Sinnott, P. Peralta, B.P. Uberuaga, C.R. Stanek, Grain boundaries in uranium dioxide: scanning electron microscopy experiments and atomistic simulations, J. Am. Ceram. Soc. 94 (6) (2011) 1893–1900, doi:10.1111/j.1551-2916.2010.04295.x.

[24] T. Harbison, Anisotropic grain boundary energy function for uranium dioxide, Brigham Young University-Idaho, 2015 Ph.D. thesis.

[25] C.B. Basak, A.K. Sengupta, H.S. Kamath, Classical molecular dynamics simulation of UO_2 to predict thermophysical properties, J Alloys Compd 360 (1) (2003) 210–216, doi:10.1016/S0925-8388(03)00350-5.

[26] G. Gottstein, L.S. Shvindlerman, L.S. Shvindlerman, Grain Boundary Migration in Metals: Thermodynamics, Kinetics, Applications, second edition, CRC Press, 2009, doi:10.1201/9781420054361.

[27] M.R. Tonks, Y. Zhang, S.B. Biner, P.C. Millett, X. Bai, Guidance to design grain boundary mobility experiments with molecular dynamics and phase-field modeling, Acta Mater 61 (4) (2013) 1373–1382, doi:10.1016/j.actamat.2012.11.014.

[28] J. Powers, A. Glaeser, Grain boundary migration in ceramics, Interface Sci. 6 (1) (1998) 23–39, doi:10.1023/A:1008656302007.

[29] A. Cheniour, M.R. Tonks, B. Gong, T. Yao, L. He, J.M. Harp, B. Beeler, Y. Zhang, J. Lian, Development of a grain growth model for U3Si2 using experimental data, phase field simulation and molecular dynamics, J. Nucl. Mater. (2020) 152069.

[30] T. Yao, K. Mo, D. Yun, S. Nanda, A.M. Yacout, J. Lian, Grain growth and pore coarsening in dense nano-crystalline UO2+x fuel pellets, J. Am. Ceram. Soc. 100 (6) (2017) 2651–2658, doi:10.1111/jace.14780.

[31] X.-M. Bai, Y. Zhang, M.R. Tonks, Testing thermal gradient driving force for grain boundary migration using molecular dynamics simulations, Acta Mater 85 (2015) 95–106, doi:10.1016/j.actamat.2014.11.019.

[32] H. Sun, C. Deng, Direct quantification of solute effects on grain boundary motion by atomistic simulations, Comput. Mater. Sci 93 (2014) 137–143.

[33] A.C.S. Sabioni, W.B. Ferraz, F. Millot, Effect of grain-boundaries on uranium and oxygen diffusion in polycrystalline UO_2, J. Nucl. Mater. 278 (2) (2000) 364–369, doi:10.1016/S0022-3115(99)00250-0.

[34] Y. Liu, B.R. Patterson, Stereological analysis of Zener pinning, Acta Mater 44 (11) (1996) 4327–4335, doi:10.1016/1359-6454(96)00107-3.

[35] A. Eivani, S. Valipour, H. Ahmed, J. Zhou, J. Duszczyk, Effect of the size distribution of nanoscale dispersed particles on the zener drag pressure, Metallurgical and Materials Transactions A 42 (4) (2011) 1109–1116.

[36] K. Chang, W. Feng, L.-Q. Chen, Effect of second-phase particle morphology on grain growth kinetics, Acta Mater 57 (17) (2009) 5229–5236.

[37] S.-J.L. Kang, Y.-I. Jung, Sintering kinetics at final stage sintering: model calculation and map construction, Acta Mater 52 (15) (2004) 4573–4578.

[38] R.L. Williamson, J. Hales, S. Novascone, M. Tonks, D. Gaston, C. Permann, D. Andrs, R. Martineau, Multidimensional multiphysics simulation of nuclear fuel behavior, J. Nucl. Mater. 423 (1–3) (2012) 149–163.

[39] M.R. Tonks, D. Andersson, S.R. Phillpot, Y. Zhang, R. Williamson, C.R. Stanek, B.P. Uberuaga, S.L. Hayes, Mechanistic materials modeling for nuclear fuel performance, Ann Nucl Energy 105 (2017) 11–24.

[40] IAEA, Improvement of Computer Codes Used for Fuel Behaviour Simulation (FUMEX-III): Report of a Coordinated Research Project 2008-2012, Technical Report IAEA-TECDOC-1697, International Atomic Energy Agency, 2008-2012.